

Four-wave Mixing of Topological Edge Plasmons in Graphene Metasurfaces

Jian Wei You,¹ Zhihao Lan,¹ and Nicolae C. Panoiu^{1*}

¹Department of Electronic and Electrical Engineering, University College London, Torrington Place, London WC1E 7JE, United Kingdom

*To whom correspondence should be addressed; E-mail: n.panoiu@ucl.ac.uk.

We study topologically-protected four-wave mixing (FWM) interactions in a plasmonic metasurface consisting of a periodic array of nanoholes in a graphene sheet, which exhibits a wide topological bandgap at terahertz frequencies upon the breaking of time-reversal symmetry by a static magnetic field. We demonstrate that due to the significant nonlinearity enhancement and large lifetime of graphene plasmons in specific configurations, a net gain of FWM interaction of plasmonic edge states within the topological bandgap can be achieved with pump power of less than 10 nW. In particular, we find that the effective waveguide nonlinearity coefficient is about $\gamma \simeq 1.1 \times 10^{13} \text{ W}^{-1} \text{ m}^{-1}$, i.e., more than ten orders of magnitude larger than that of commonly used, highly nonlinear silicon photonic nanowires. These findings could pave a new way for developing ultra-low-power-consumption, highly-integrated and robust active photonic systems at deep-subwavelength scale for applications in quantum communications and information processing.

Introduction

In the past decade, topological photonics has emerged as a rapidly burgeoning field of exploration of topological physics in the context of photonics. This area of research began with the theoretical work by Haldane and Raghu (*1, 2*), where they constructed an analogue of quantum Hall edge states in photonic crystals based on magneto-optical media and observed topological edge modes within the corresponding photonic bandgaps. Shortly afterwards, an experimental realization and observation of such topological edge modes in a magneto-optical photonic crystal was reported in the microwave regime (*3*). Since then, there has been increasing interest in implementing in photonics topological states of matter as well as developing new ideas specific to topological photonics (*4–8*).

In addition to new perspectives brought in fundamental science, topological photonics also offers a broad array of potential applications for novel photonic devices, as its exotic features have already prompted the reexamination of some traditional views on light manipulation and propagation. For instance, reducing back-reflection is a major challenge in optical waveguides, and in this context the unidirectional topological waveguide (*9–11*) is an ideal light transport device in integrated photonics, as it could transmit light without backscattering even in the presence of inherent structural disorder. Moreover, some new concepts of topological photonics have also led to the development of novel photonic devices, such as optical isolator (*12, 13*), robust delay lines (*14, 15*), signal switches (*16*), non-reciprocal devices (*17–19*), and topological lasers (*20, 21*).

Most of the previous studies have focused on linear topological photonic systems; however, topological physics could also play an important role in the nonlinear regime, leading to novel collective phenomena and strongly-correlated states of light (*8*). For instance, a topological source of quantum light has recently been realized in a nonlinear photonic system, which paves

a new way for the development of robust quantum photonic devices (22).

Results

The system

We study a topologically-protected nonlinear four-wave mixing process in a graphene plasmonic system. Graphene distinguishes itself as an ideal platform to study nonlinear topological photonics in several key aspects: First, graphene exhibits remarkably large nonlinearity over a broad spectral range, from terahertz to visible light. In particular, it has been shown (23) that graphene in a strong magnetic field has the largest third-order susceptibility of all known materials. Second, some recent studies (24, 25) showed that topologically protected one-wave edge plasmons can be realized in graphene metasurfaces. In addition to the typical plasmonic effects, such as local-field enhancement and field confinement, the local field can be further confined to the edge of the graphene plasmonic system, leading to a dramatic enhancement of the nonlinear optical response of the graphene system. Third, phase-matching is a crucial condition in nonlinear frequency mixing processes. In contrast to the frequently used bulk modes (22), where several modes with different wave vectors usually exist at a given frequency, a topological edge mode has a unique wave vector at a fixed frequency, thus the phase-matching condition is insensitive to the way one excites the system, as in this case only a single mode could be excited at one frequency. These important features make graphene plasmonic systems particularly appealing in the design of highly integrated nonlinear topological nanophotonic devices.

The nonlinear system explored in this work is illustrated in Fig. 1. A graphene plasmonic metasurface consisting of a periodic nanohole array with hexagonal symmetry is placed in a static magnetic field. Due to the time-reversal-symmetry breaking induced by the magneto-optical response of graphene under an external magnetic field, this plasmonic system could possess a topological bandgap. After a geometry optimization, the topological bandgap could

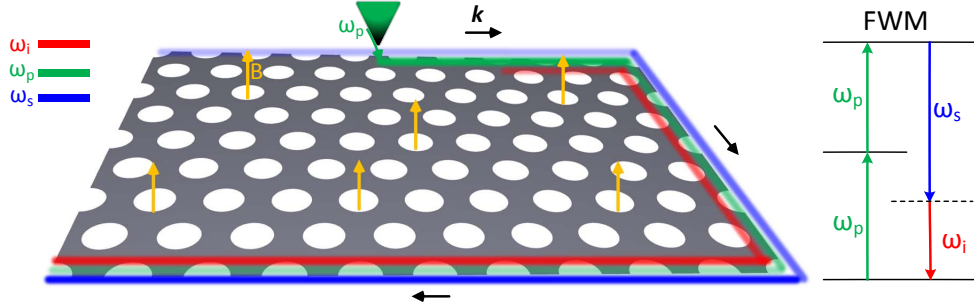


Figure 1: Four-wave mixing of topologically protected one-way edge plasmons in a graphene metasurface consisting of a periodic nanohole array with hexagonal symmetry in a static magnetic field and the corresponding energy level diagram of the four-wave mixing process.

become wide enough so that optical modes taking part in a four-wave mixing (FWM) process can readily fit in it. In order to induce a FWM process, the system is excited by an external source at the pump frequency ω_p , as illustrated in Fig. 1. Due to the strong third-order nonlinearity of graphene, a degenerate FWM process could take place, where two photons in a pump mode will generate a pair of photons at the signal and idler frequencies, ω_s and ω_i , respectively. As a result, the energy of the pump wave (green) in Fig. 1 is transferred to the (seeded) signal (blue) and idler (red) modes, leading to the pump decay and the amplification of the signal and idler. More importantly, this degenerate FWM process is topologically protected by the chiral nature of the edge plasmons.

Topological bands of the graphene plasmonic system: linear response

We first study the linear optical response of our graphene plasmonic system by calculating its photonic band structure using a numerical approach based on the finite-element method (FEM). The unit cell (with lattice constant a and air hole radius r) and the first Brillouin zone of the system used in our simulations are shown in Fig. 2(a) and 2(b), respectively. The band diagrams of the system ($a = 400$ nm, $r = 120$ nm) at different magnetic field $B = 0, 2, 5, 7, 10$ T are presented in Fig. 2(c), where the parameters of the graphene are set to be $E_F = 0.2$ eV, $v_F \approx$

10^6 m s^{-1} and $\tau = 50 \text{ ps}$ (see the section of Materials and Methods for details).

There are several notable features of the results presented in Fig. 2(c). First, without the external magnetic field ($B = 0$), due to the hexagonal symmetry of the metasurface structure, Dirac cones that are protected by the parity (P) inversion and time-reversal (T) symmetries exist at K and K' symmetry points of the Brillouin zone (24). Second, in the presence of the magnetic field ($B \neq 0$), the time-reversal symmetry of the system is broken and, consequently, the Dirac cones are gapped out resulting in a topological nontrivial bandgap. Moreover, the width $\Delta\nu$ of this bandgap increases as the amplitude of the magnetic field increases.

To confirm the topological nature of the bandgap, we illustrate the emergence of the edge modes within the bandgap for a finite size system along the y -axis, i.e., the number of unit cells along this direction is finite (chosen to be 20 in our FEM simulations), whereas the system is periodic along the x -axis [in the FEM simulations, periodic boundary conditions are imposed at the left and right boundaries along the x -axis, see Fig. 3(a)]. The supercell for this finite

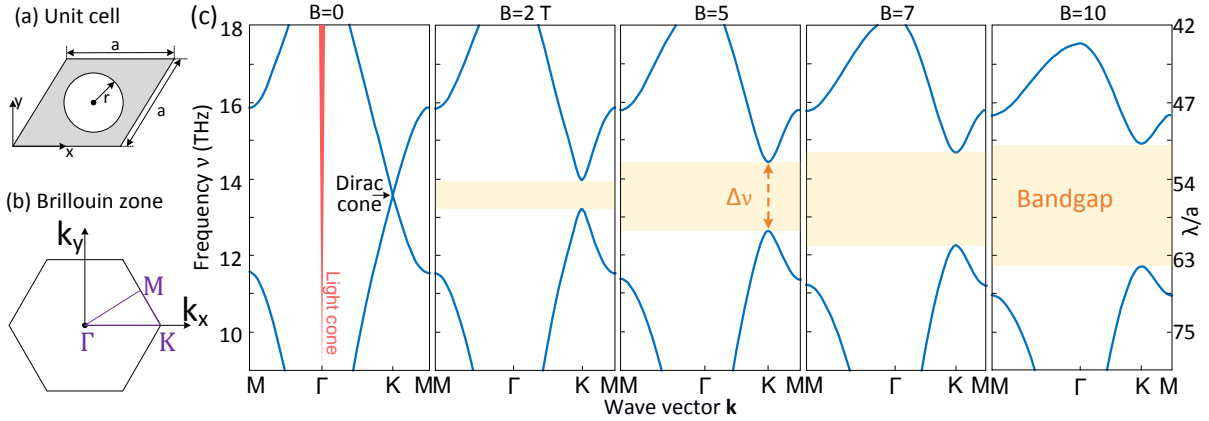


Figure 2: Band diagrams of the graphene plasmonic metasurface. (a) Unit cell and (b) the first Brillouin zone of the metasurface. (c) Band diagrams of the metasurface at $B = 0, 2, 5, 7, 10 \text{ T}$. As the Dirac cone is below the air light cone, surface plasmons can exist around this cone at deep-subwavelength scale ($\lambda/a > 40$). Moreover, a topological bandgap is opened in the presence of an external static magnetic field.

system is shown by a green rectangle in Fig. 3(a), whose width and length are a and $b = \sqrt{3}a$, respectively.

The projected band diagrams along k_x , determined for $B = 0, 2, 5, 7, 10$ T, are depicted in Fig. 3(b). First, similar to what we observed in Fig. 2(c), a bandgap opens when one applies an external static magnetic field ($B \neq 0$), with the gap width $\Delta\nu$ increasing as the amplitude of magnetic field increases. However, different from the band diagrams of an infinite graphene metasurface shown in Fig. 2(c), in the band diagrams of Fig. 3(b) there are two additional edge modes at the top (red) and bottom (blue) boundaries of the finite graphene system. These two edge modes connect the bulk bands located above and below the bandgap, and cannot be moved out of the bandgap into the bulk bands as long as the bandgap exists. In other words, they are robust and defect-immune, guaranteed by the topological protection of the bandgap.

One can also calculate the gap Chern number, which is a topological invariant that charac-

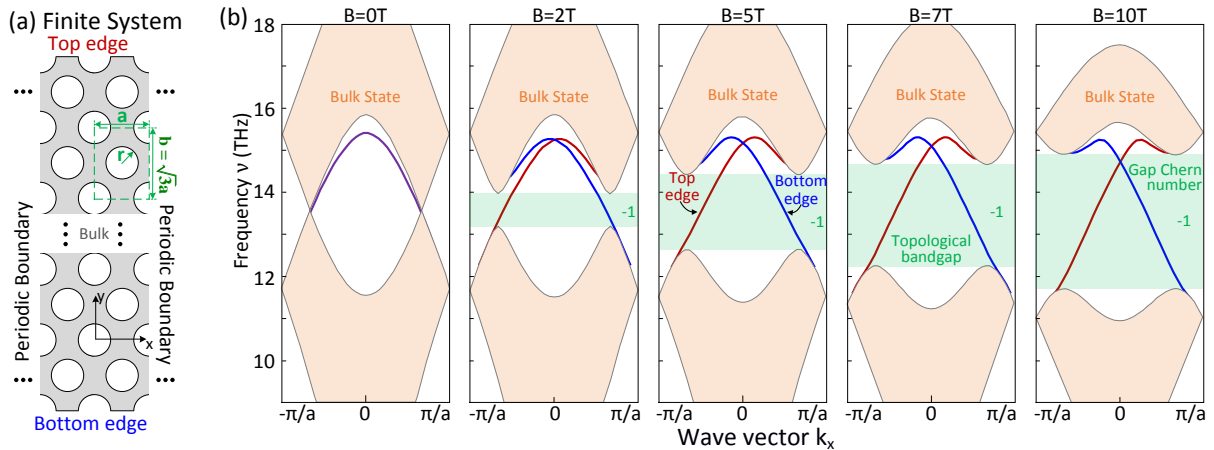


Figure 3: **Band diagrams of a finite graphene metasurface.** (a) Geometry of the finite graphene metasurface, where the number of unit cells (green dashed frame) is finite along the y -axis and infinite along the x -axis. (b) Projected band diagrams of the metasurface at $B = 0, 2, 5, 7,$ and 10 T, where the edge modes on the top and bottom boundaries are depicted by red and blue curves, respectively. Since the gap Chern number characterizes the number of edge modes in the gap, there is a single edge mode at each boundary.

terizes the topological properties of the bandgap, to further confirm that the bandgap discussed above is topologically nontrivial and that these edge modes are topological modes (24). To this end, we present in Fig. 3(b) (green) the calculated gap Chern number. Since the gap Chern number is -1 (the magnitude indicates the number of topological edge modes, whereas the sign shows the direction of propagation), there is only one topologically protected edge mode for each edge termination. In other words, our graphene structure supports modes that can exhibit unidirectional and defect-immune propagation features along the top and bottom edges. Moreover, the property of unidirectional propagation of the edge modes is also illustrated by the slope of the edge modes in the bandgap, as their group velocity, $v_g = \partial\omega/\partial k$, within the topological bandgap is either positive (top edge) or negative (bottom edge).

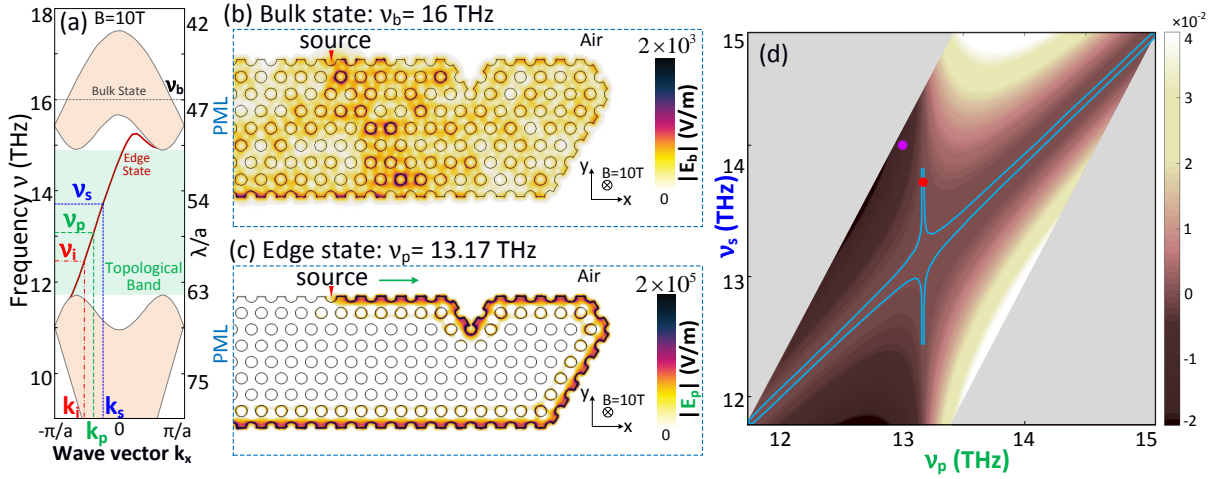


Figure 4: **Nonlinear edge-mode interaction and four-wave mixing within a wide topological bandgap.** (a) Band diagram of the graphene metasurface at $B = 10$ T. (b) Field profile of a bulk mode excitation at $\nu_b = 16$ THz, showing that the optical field spreads throughout the bulk region. (c) Field profile of an edge mode excitation at $\nu_b = 13.17$ THz, illustrating its unidirectional and defect-immune propagation along the system edge ($\tau \rightarrow \infty$). (d) Dispersion map of the normalized wave vector mismatch $\Delta\kappa$. The blue contour is defined by the condition $\Delta\kappa = 10^{-5}$, whereas the red and magenta dots correspond to a nearly phase-matched ($\Delta\kappa = 5.16 \times 10^{-6}$) and a phase-mismatched ($\Delta\kappa = 1.75 \times 10^{-2}$) FWM process, respectively.

In order to gain deeper physical insights into the physical properties of plasmonic bulk and edge modes of the graphene metasurface, the near field distribution of these modes propagating in a finite graphene plasmonic metasurface [4 unit cells along the y -axis and about 15 unit cells along the x -axis, as per Figs. 4(b) and 4(c)], is studied by using full-wave FEM simulations. In the simulations, a perfectly-matched layer (PML) is used at the left side of the graphene structure, whereas at the other sides we imposed scattering boundary conditions so as to mimic infinite air space. In order to excite specific modes of this finite graphene system, an electric source ($E_0 = 2 \times 10^4 \text{V/m}$) depicted by a red triangle in Fig. 4(b) is used.

In the case of the bulk mode, we choose the source frequency $\nu_b = 16 \text{ THz}$, which belongs to the bulk region [see Fig. 4(a)]. As expected, the corresponding optical field spreads throughout the graphene structure [see Fig. 4(b)], which proves that indeed a bulk mode is excited in this case. It should be noted that, due to the plasmonic characteristics of the graphene bulk modes, their optical field is tightly confined at the surface of the graphene metasurface.

In the case of the excitation of an edge mode, we choose a frequency in the bandgap, $\nu_p = 13.17 \text{ THz}$, so that at this frequency only the edge mode exists, as per Fig. 4(a). The corresponding field profile generated by the source in the finite system, presented in Fig. 4(c), illustrates several notable features. Thus, the optical field does not penetrate in the bulk region and only propagates unidirectionally along the edge of the graphene metasurface. In addition, because of the chiral nature of the edge mode, this unidirectional propagation is robust against structural defects, which allows it to circumvent defects (e.g., sharp bends) without producing back-scattering. These features prove that the edge modes within the topological bandgap in Fig. 4(a) are indeed topologically protected. Last but not least, we note that in addition to the plasmonic field confinement effect illustrated in Figs. 4(b) and 4(c), the optical field of the edge modes is further confined to the edge of the system, which is particularly important when one seeks to enhance nonlinear optical interactions such as FWM.

Nonlinear interaction of edge states: Four-wave mixing

Comparing Figs. 4(b) and 4(c), one can see that, in the case of the edge mode, the plasmon-induced field-enhancement effect quantified by the ratio $|E_e|_{max}/E_0$, is two orders of magnitude stronger than that in the case of bulk mode $|E_b|_{max}/E_0$, namely $|E_e|_{max}/|E_b|_{max} > 100$. Moreover, the results in Fig. 4(a) show that at a particular frequency there is only a single edge mode, with a unique wave vector, whereas several different bulk modes can be excited at one frequency. The former effect is important in enhancing the nonlinear optical interactions, whereas the latter one is particularly useful for engineering physical configurations in which phase-matching in FWM is achieved.

In order to illustrate these ideas, in what follows we analyze the circumstances in which the phase-matching condition in a degenerate FWM of one-way edge modes can be fulfilled. To this end, we calculate the normalized wave vector mismatch, defined as $\Delta\kappa = a\Delta k = a(2k_p - k_s - k_i)$, corresponding to a FWM process in which a pump edge mode with wave vector \mathbf{k}_p gives rise to signal and idler edge modes with wave vectors \mathbf{k}_s and \mathbf{k}_i , respectively. In particular, the exchange of energy among the interacting waves is most efficient when the phase-matching condition $\Delta\kappa = 0$ is satisfied. Unlike the wave vector, the energy is conserved in the FWM process, meaning $2\nu_p = \nu_s + \nu_i$.

Starting from the mode dispersion curves of the topological edge modes presented in Fig. 4(a), and using the energy conservation relation that characterizes the FWM process, the corresponding dispersion map of the normalized wave vector mismatch $\Delta\kappa$ is calculated numerically and depicted in Fig. 4(d). In particular, for the sake of a better quantitative understanding of the energy conversion efficiency of the FWM process, we also show in this figure the contour defined by $\Delta\kappa = 10^{-5}$. More specifically, for frequencies inside the domain defined by this contour, energy is transferred from the pump to the signal and idler over a distance larger than $\sim 10^5\pi$ lattice constants.

In order to validate the conclusions derived from the dispersion map of $\Delta\kappa$, we perform full-wave simulations of the nonlinear dynamics of the interacting edge modes. To this end, we chose a point indicated with a red dot in Fig. 4(d), characterized by $\nu_p = 13.17$ THz, $\nu_s = 13.72$ THz, and $\nu_i = 12.62$ THz, and for which the FWM interaction is nearly phase-matched ($\Delta\kappa = 5.16 \times 10^{-6}$). Moreover, we considered a seeded FWM process in which the input intensity of the signal is much smaller than that of the pump, whereas the input intensity of the idler is set to zero. Specifically, in our FEM simulations we set the source input field amplitudes at the three frequencies $|E_p| = 2 \times 10^4$ V m⁻¹, $|E_s| = 4 \times 10^2$ V m⁻¹, and $|E_i| = 0$. Finally, the nonlinearity of graphene under the influence of a magnetic field of 10 T is described by a third-order susceptibility with value of $\chi^{(3)} = 5 \times 10^{-10}$ m² V⁻² (23).

Using the procedure we just described, we have computed the near-field profiles at the frequencies of the pump, signal, and idler, the results of these simulations being summarized in Fig. 5. In these calculations graphene losses are neglected by setting $\tau \rightarrow \infty$. It can be seen in Figs. 5(a) and 5(b) that, as the result of the nonlinear FWM interaction, the signal is amplified upon propagation whereas an edge mode is generated at the idler frequency [note that in Fig. 5(b) there is no external source at the idler frequency]. Equally important, since the frequency of all the interacting edge modes are located in the topological bandgap, both signal and idler modes are topologically protected and exhibit unidirectional and defect-immune propagation along the system edge.

The FWM process can be further, quantitatively investigated by calculating the dependence on the propagation distance of the power carried by the three edge modes. The mode power is calculated by integrating the corresponding Poynting vector across the transverse section. The results of these calculations are summarized in Figs. 5(c) and 5(d), and correspond to the case of near phase-matching discussed above and a case when the FWM process is not phase-matched, respectively. In the latter case, the system parameters are $\nu_p = 13.03$ THz, $\nu_s = 14.05$ THz,

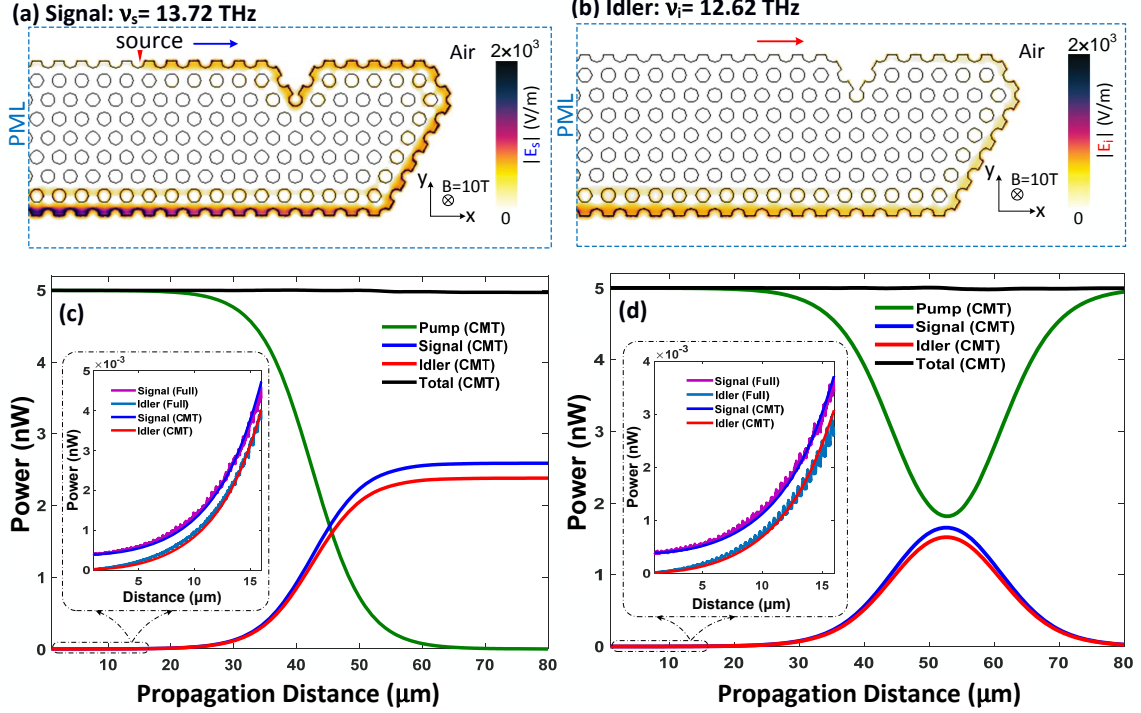


Figure 5: **Topologically-protected FWM process in a graphene metasurface.** (a) The field profile at the signal frequency, $\nu_s = 13.72$ THz. (b) The field profile at the idler frequency, $\nu_i = 12.62$ THz. (c) Dependence on the propagation distance of the mode power of the pump, signal, and idler corresponding to the field profiles shown in Fig. 5(a) and Fig. 5(b), determined using the CMT when the FWM process is phase-matched. Also shown in the inset are the same mode powers determined using the CMT and full-wave simulations. The black curve corresponds to the total power and shows that the energy is conserved in the FWM interaction. (d) The same as in Fig. 5(c), but corresponding to a case when the FWM interaction is not phase-matched.

$\nu_i = 12.01$ THz, and $\Delta\kappa = 1.75 \times 10^{-2}$ [the magenta point in Fig. 4(d)].

There are several important ideas revealed by the results presented in Figs. 5(c) and 5(d). First, the power of both the signal and idler modes is amplified upon propagation, due to the energy conversion from the pump mode. Second, the growth rate of signal and idler modes in the case of the nearly phase-matched FWM is larger than that corresponding to the case when the FWM interaction is not phase-matched, which means that the energy conversion is more efficient in the former case. Third, there is a very good agreement between the predictions

of the coupled-mode theory (CMT) (see Supplementary Materials for details) and the results obtained using full-wave simulations of the nonlinear mode interaction, despite the fact that the optical fields at the three frequencies are strongly confined at deep-subwavelength scale and significantly enhanced.

Importantly, our CMT predicts that the effective nonlinear FWM coefficient is $\gamma_{FWM} \approx 2.4 \times 10^{13} \text{ W}^{-1} \text{ m}^{-1}$ (see Supplementary Materials), which is more than ten orders of magnitude larger than that of silicon photonic wire waveguides (26, 27). To the best of our knowledge, this is the largest nonlinear FWM coefficient reported in a nonlinear optical system to date. This remarkable result is a consequence of the particularly large third-order susceptibility of graphene, which is further enhanced by the plasmon-induced enhancement and extreme confinement of the optical field of the edge modes. In particular, the size of the unit cell of the graphene metasurface is much smaller than the operating wavelength, namely $\lambda/a > 50$ in our FWM process, a notable feature that can facilitate the design of low-power, ultracompact active photonic nanodevices.

The radiation loss of the edge modes of the graphene metasurface can be neglected because, as we just discussed, they are strongly confined. The intrinsic loss, however, has to be taken into account in practical applications. To study its influence on the FWM interaction, a finite plasmon lifetime τ is considered in Eq. 2 and Eq. 3. Similarly to the lossless case, we determined the dependence of the power of the interacting edge modes on the propagation distance, the corresponding results of this analysis being presented in Fig. 6.

Typically, the plasmon lifetime is determined by the plasmon-phonon coupling and varies from 0.1 ps to 1 ps (28). This loss can be reduced if exfoliated graphene is placed onto a boron nitride substrate (29), which leads to a lifetime as large as 3 ps. Moreover, recent experiments (30,31) have demonstrated that an external magnetic field can also strongly increase the plasmon lifetime, as in this case the two-dimensional surface plasmon can be effectively transformed

into a one-dimensional-like edge plasmon. Specifically, it has been shown that by applying an external magnetic field the plasmon lifetime can be readily increased to 50 ps (31).

One remarkable conclusion of the analysis of the FWM interaction of edge modes of lossy graphene is that net signal gain can be achieved if the life-time $\tau \gtrsim 2.5$ ps. In fact, this is the first plasmonic system in which net gain can be achieved without incorporating in the system gain optical media. Indeed, it can be seen in Fig. 6 that whereas the pump decays for all values of the plasmon life-time, due to the combined contributions of the graphene loss and energy transfer mediated by the FWM interaction, the signal power increases monotonously if $\tau \gtrsim 2.5$ ps. The idler, on the other hand, shows a more complex dynamics. Thus, irrespective of the value of the life-time, at the beginning of the nonlinear interaction the power in the idler builds up over a certain distance. After this amplification stage the power in the idler decays monotonously if $\tau \lesssim 2.5$ ps, because the pump power is no longer large enough to sustain the amplification of

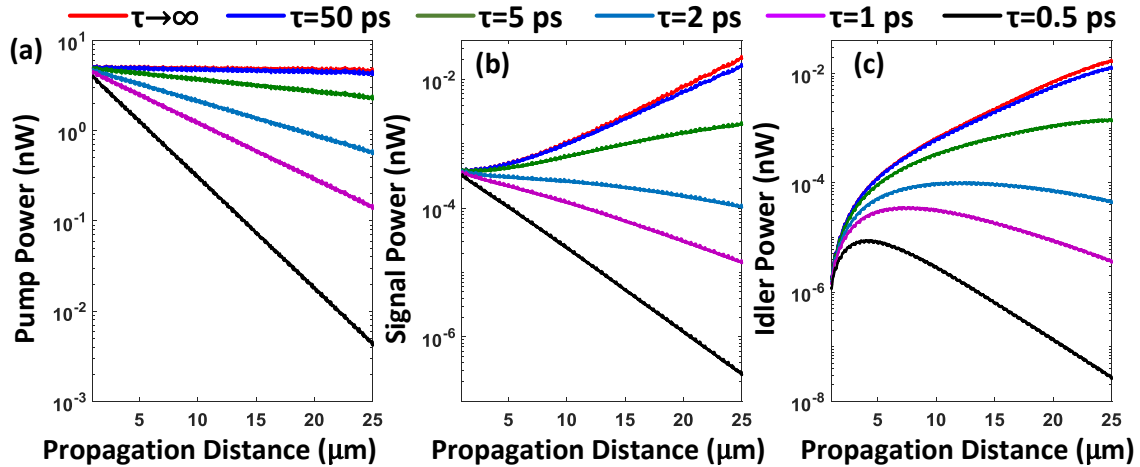


Figure 6: **Influence of loss on the topologically-protected FWM process in graphene meta-surface at $B = 10$ T.** (a), (b), (c) Dependence on the propagation distance of the power of the pump, signal, and idler edge modes, respectively, corresponding to a phase-matched FWM process determined for different values of the loss rate. Owing to the particularly large value of the FWM coefficient, net gain (the FWM gain overcompensates the loss) can be achieved as long as $\tau \gtrsim 2.5$ ps.

the idler, whereas if $\tau \gtrsim 2.5$ ps the power in the idler mode increases monotonously over the entire distance considered in our simulations.

Conclusion

Using rigorous full-wave simulations supported by a coupled-mode theory we have demonstrated a topologically protected nonlinear four-wave mixing process in a patterned graphene plasmonic metasurface. In particular, we have shown that a topological bandgap as wide as several THz can be created in the metasurface under a strong static magnetic field. Moreover, the analysis of the dispersion properties of the topologically-protected edge modes located in the bandgap reveals that four-wave mixing interaction is efficiently phase-matched in a large domain of the parameter space of the system. The near-field profiles of the interacting edge modes show unidirectional and defect-immune propagation, hence demonstrating that the four-wave mixing process is topologically protected. Remarkably, our study also reveals that, due to an unusually large value of the four-wave mixing nonlinear coefficient and the large field enhancement at plasmon resonances, the four-wave mixing interaction produces net gain even when plasmon losses in graphene are rigorously taken into account. This striking property of four-wave mixing of topological edge modes of graphene metasurfaces might play an important rôle in the development of new ultracompact and topologically-protected active photonic systems.

Materials and Methods

In our modeling of an infinite graphene metasurface, periodic boundary conditions are used for the four edges of the unit cell depicted in Fig. 2(a). At infrared and terahertz frequencies, graphene placed in a static magnetic field can be characterized as an electrically gyrotropic

material (32–34), whose surface conductivity tensor can be represented as:

$$\boldsymbol{\sigma}_s = \begin{bmatrix} \sigma_L & \sigma_H \\ -\sigma_H & \sigma_L \end{bmatrix}, \quad (1)$$

where the diagonal elements (longitudinal conductivity, σ_L) and the off-diagonal elements (Hall conductivity, σ_H) can be determined using Kubo's formalism (35). At room temperature and for frequencies below the visible-light region, the longitudinal and Hall conductivities are given by (24, 25):

$$\sigma_L = \sigma_0 \frac{1 - i\omega\tau}{(\omega_c\tau)^2 - (i + \omega\tau)^2}, \quad (2)$$

$$\sigma_H = -\sigma_0 \frac{\omega_c\tau}{(\omega_c\tau)^2 - (i + \omega\tau)^2}, \quad (3)$$

where $\sigma_0 = e^2 E_F \tau / (\pi \hbar^2)$, τ is the relaxation time (plasmon lifetime), $\omega_c \approx e B_\perp v_F^2 / E_F$ is the cyclotron frequency, with B_\perp , v_F , and E_F being the external static magnetic field perpendicular onto the graphene surface, the graphene Fermi velocity, and the Fermi energy, respectively.

The surface conductivities in Eq. 2 and Eq. 3 show that the graphene under a static magnetic field ($B_\perp \neq 0$) is anisotropic, lossy, and dispersive. As a consequence, most of the traditional electromagnetic eigenmode solvers based on the plane wave expansion method cannot be used to determine the photonic band structure. In order to circumvent this problem, we used the numerical solver of Comsol based on the FEM method to calculate the band diagrams of the graphene metasurfaces investigated in this study. In our full-wave simulations, electric sources are placed at positions with low symmetry, so that all modes are excited. Moreover, multiple probe monitors are placed at low-symmetry locations, too, to determine the mode frequencies.

In the nonlinear simulations, three nonlinear surface currents are defined in the Comsol software, namely one for the pump frequency (ν_p), one for the signal frequency (ν_s), and one for the idler frequency (ν_i). These nonlinear currents are coupled, as described by the following equations:

$$J_p^{surf} = 6\sigma_{p,surf}^{(3)} E_s E_i E_p^*, \quad (4)$$

$$J_s^{surf} = 3\sigma_{s,surf}^{(3)} E_p E_p E_i^*, \quad (5)$$

$$J_i^{surf} = 3\sigma_{i,surf}^{(3)} E_p E_p E_s^*. \quad (6)$$

Here, the third-order surface conductivity is defined as $\sigma_{\alpha,surf}^{(3)} = -i\epsilon_0\omega_\alpha h_{eff}\chi^{(3)}$, $\alpha = p, s, i$, where $\chi^{(3)}$ is the third-order bulk susceptibility and the thickness of graphene is assumed to be $h_{eff} = 0.3 \text{ nm}$ (23). Moreover, the electric fields E_α , $\alpha = p, s, i$, are the amplitudes of the pump, signal, and idler, respectively. More details about the nonlinearity of magnetized graphene and the coupled-mode theory describing the FWM interaction of graphene edge modes can be found in the Supplementary Materials.

References

1. F. D. M. Haldane, S. Raghu, Possible realization of directional optical waveguides in photonic crystals with broken time-reversal symmetry. *Phys. Rev. Lett.* **100**, 013904 (2008).
2. S. Raghu, F. D. M. Haldane, Analogs of quantum-hall-effect edge states in photonic crystals, *Phys. Rev. A* **78**, 033834 (2008).
3. Z. Wang, Y. Chong, J. D. Joannopoulos, M. Soljacic, Observation of unidirectional backscattering-immune topological electromagnetic states. *Nature* **461**, 772-775 (2009).
4. L. Lu, J. D. Joannopoulos, M. Soljacic, Topological photonics. *Nat. Photonics* **8**, 821 (2014).
5. L. Lu, J. D. Joannopoulos, M. Soljacic, Topological states in photonic systems. *Nat. Phys.* **12**, 626 (2016).
6. A. B. Khanikaev, G. Shvets, Two-dimensional topological photonics. *Nat. Photonics* **11**, 763 (2017).

7. C. Liu, W. Gao, B. Yang, S. Zhang, Disorder-induced topological state transition in photonic metamaterials. *Phys. Rev. Lett.* **119**, 183901 (2017).
8. T. Ozawa, H. M. Price, A. Amo, N. Goldman, M. Hafezi, L. Lu, M. Rechtsman, D. Schuster, J. Simon, O. Zilberberg, I. Carusotto, Topological photonics. *Rev. Mod. Phys.* **91**, 015006 (2019).
9. Z. Wang, Y. D. Chong, J. D. Joannopoulos, M. Soljacic, Reflection-free one-way edge modes in a gyromagnetic photonic crystal. *Phys. Rev. Lett.* **100**, 013905 (2008).
10. Y. Yang, Y. Poo, R. X. Wu, Y. Gu, P. Chen, Experimental demonstration of one-way slow wave in waveguide involving gyromagnetic photonic crystals. *Appl. Phys. Lett.* **102**, 231113 (2013).
11. S. Mittal, J. Fan, S. Faez, A. Migdall, J. M. Taylor, M. Hafezi, Topologically robust transport of photons in a synthetic gauge field. *Phys. Rev. Lett.* **113**, 087403 (2014).
12. D. D. Solnyshkov, O. Bleu, G. Malpuech, Topological optical isolator based on polariton graphene. *Appl. Phys. Lett.* **112**, 031106 (2018).
13. C. He, X. L. Chen, M. H. Lu, X. F. Li, W. W. Wan, X. S. Qian, R. C. Yin, Y. F. Chen, Tunable one-way cross-waveguide splitter based on gyromagnetic photonic crystal. *Appl. Phys. Lett.* **96**, 111111 (2010).
14. M. Hafezi, S. Mittal, J. Fan, A. Migdall, J. M. Taylor, Imaging topological edge states in silicon photonics. *Nat. Photon.* **7**, 1001-1005 (2013).
15. X. Cheng, C. Jouvaud, X. Ni, S. H. Mousavi, A. Z. Genack, A. B. Khanikaev, Robust reconfigurable electromagnetic pathways within a photonic topological insulator. *Nat. Mater.* **15**, 542-548 (2016).

16. X. Zang, C. Jiang, Edge mode in nonreciprocal photonic crystal waveguide: manipulating the unidirectional electromagnetic pulse dynamically. *J. Opt. Soc. Am. B* **28**, 554-557 (2011).
17. J. X. Fu, R. J. Liu, Z. Y. Li, Robust one-way modes in gyromagnetic photonic crystal waveguides with different interfaces. *Appl. Phys. Lett.* **97**, 041112 (2010).
18. J. X. Fu, J. Lian, R. J. Liu, L. Gan, Z. Y. Li, Unidirectional channel-drop filter by one-way gyromagnetic photonic crystal waveguides. *Appl. Phys. Lett.* **98**, 211104 (2011).
19. W. Qiu, Z. Wang, M. Soljacic, Broadband circulators based on directional coupling of one-way waveguides. *Opt. Express* **19**, 22248-22257 (2011).
20. B. Bahari, A. Ndao, F. Vallini, A. El Amili, Y. Fainman, B. Kante, Nonreciprocal lasing in topological cavities of arbitrary geometries. *Science* **358**, 636-640 (2017).
21. P. St-Jean, V. Goblot, E. Galopin, A. Lemaitre, T. Ozawa, L. Le Gratiet, I. Sagnes, J. Bloch, A. Amo, Lasing in topological edge states of a one-dimensional lattice. *Nat. Photon.* **11**, 651-656 (2017).
22. S. Mittal, E. A. Goldschmidt, M. Hafezi, A topological source of quantum light. *Nature* **561**, 502-506 (2018)
23. X. Yao, A. Belyanin, Giant optical nonlinearity of graphene in a strong magnetic field. *Phys. Rev. Lett.* **108**, 255503 (2012).
24. D. Jin, T. Christensen, M. Soljacic, N. X. Fang, L. Lu, X. Zhang, Infrared topological plasmons in graphene. *Phys. Rev. Lett.* **118**, 245301 (2017).
25. D. Pan, R. Yu, H. Xu, F. J. G. de Abajo, Topologically protected Dirac plasmons in a graphene superlattice. *Nat. Commun.* **8**, 1243 (2017).

26. S. Lavdas, N. C. Panoiu, Theory of pulsed four-wave mixing in one-dimensional silicon photonic crystal slab waveguides. *Phys. Rev. B* **93**, 115435 (2016).
27. M. P. Nielsen, X. Shi, P. Dichtl, S. A. Maier, R. F. Oulton, Giant nonlinear response at a plasmonic nanofocus drives efficient four-wave mixing. *Science*, **358**, 1179 (2017).
28. T. Low, P. Avouris, Graphene plasmonics for terahertz to mid-infrared applications. *ACS Nano*, **8**, 1086 (2014).
29. C. R. Dean, A. F. Young, I. Meric, C. Lee, L. Wang, S. Sorgenfrei, K. Watanabe, T. Taniguchi, P. Kim, K. L. Shepard, J. Hone, Boron Nitride substrates for high-quality graphene electronics. *Nat. Nanotechnol.* **5**, 722 (2010).
30. H. Yan, Z. Li, X. Li, W. Zhu, P. Avouris, F. Xia, Infrared spectroscopy of tunable Dirac terahertz mMagneto-plasmons in graphene. *Nano Lett.* **12**, 3766 (2012).
31. I. Petkovic, F. I. B. Williams, K. Bennaceur, F. Portier, P. Roche, D. C. Glattli, Carrier drift velocity and edge magnetoplasmons in graphene. *Phys. Rev. Lett.* **110**, 016801 (2013).
32. I. Crassee, J. Levallois, A. L. Walter, M. Ostler, A. Bostwick, E. Rotenberg, T. Seyller, D. Van Der Marel, A. B. Kuzmenko, Giant Faraday rotation in single-and multilayer graphene. *Nat. Phys.* **7**, 48 (2011).
33. A. Ferreira, N. M. R. Peres, A. C. Neto, Confined magneto-optical waves in graphene. *Phys. Rev. B* **85**, 205426 (2012).
34. J. W. You, S. R. Bongu, Q. Bao, N. C. Panoiu. Nonlinear optical properties and applications of 2D materials: theoretical and experimental aspects. *Nanophotonics* **8**, 63 (2019).
35. M. Dressel, G. Gruner, *Electrodynamics of solids*. Cambridge,U.K.: Cambridge Univ. Press, 2002.

36. B. E. A. Saleh, M. C. Teich, Fundamentals of Photonics (Wiley Series in Pure and Applied Optics). (Wiley-Blackwell; 2Rev Ed edition 2007).

Acknowledgments

Funding: This work was supported by European Research Council (ERC), Grant Agreement no. ERC-2014-CoG-648328.

Contributions: N.C.P. conceived the idea and supervised the project. J.W.Y. and Z.L. performed the numerical simulations. All authors contributed to the preparation of the manuscript.

Competing interests: The authors declare that they have no competing interests.

Data and materials availability: All data needed to evaluate the conclusions in the paper are present in the paper and/or the Supplementary Materials. Additional data related to this paper may be requested from the authors.